Supporting Information for

Extreme Weather Variability on Hot Rocky Exoplanet 55 Cancri e Explained by Magma Temperature-Cloud Feedback

Kaitlyn Loftus, Yangcheng Luo, Bowen Fan, and Edwin Kite

Yangcheng Luo
E-mail: yangcheng.luo@lmd.ipsl.fr

This PDF file includes:

Supporting Information Text

Role of lag d in variability

In this section, we (numerically) demonstrate that non-steady state solutions (i.e., variability) require a non-zero time lag d for vapor at the surface to become condensed cloud particles in the atmosphere. In order to test the behavior of our model with no lag, we need to reformulate the governing equations to remove division by d. We return to our model's governing equations before non-dimensionalization by d: main text Eqs. (6) and (12). We define three bulk parameters from these equations, analogous to the three bulk parameters defined from the equations with non-dimensionalized time:

$$\Pi_1' = \frac{3k_1 M_\mathrm{v}}{2gM_\mathrm{air}\rho_\mathrm{c} r_\mathrm{c} \tau_\mathrm{ascent}}, \quad [1]$$

$$\Pi_2' = \frac{2k_2 g^2 M_\mathrm{air}\rho_\mathrm{c} r_\mathrm{c}^2}{9R^* T_0 \eta}, \quad [2]$$

and

$$\Pi_3' = c_p \rho_\mathrm{m} H_\mathrm{mix}. \quad [3]$$

Note, τ_ascent in the expression for Π_1' is a timescale for vertical transport. Previously we assumed this timescale to be d. For the purpose of this analysis, we emphasis the role of d in coupling the magnitude of vapor supply to an earlier surface temperature rather than its secondary role in Π_1 as the supply timescale. (A more complex model could separate these timescales.) Here to prevent an unphysical infinite vapor supply, we assume $\tau_\mathrm{ascent} = 1$ hour from the lower bound on d. We estimate the possible ranges of the revised bulk parameters as 1.75×10^{-7} – 7.09×10^{-2} Pa^{-1} s^{-1} for Π_1', 1.27×10^{-11} – 5.94×10^{-3} s^{-1} for Π_2', and 2.38×10^{6} – 6.61×10^{9} kg s^{-2} K^{-1} for Π_3'.

Setting the lag to zero in the Clausius-Clapeyron expression of $\mathrm{d}\tau_\mathrm{SW}/\mathrm{d}t$ (i.e., $T_\mathrm{surf}|_{t-d} = T_\mathrm{surf}|_t$) and substituting the new bulk parameters, main text Eqs. (6) and (12) can be rewritten as

$$\frac{\mathrm{d}\tau_\mathrm{SW}}{\mathrm{d}t} = \Pi_1' p_\mathrm{ref} \exp\left(-\frac{T_\mathrm{ref}}{T_\mathrm{surf}}\right) - \Pi_2' \tau_\mathrm{SW} \quad [4]$$

and

$$\frac{\mathrm{d}T_\mathrm{surf}}{\mathrm{d}t} = \frac{S_0/(1+\alpha\tau_\mathrm{SW}) + \varepsilon_\mathrm{cloud}\sigma T_{\mathrm{cloud}\downarrow}^4 - \sigma T_\mathrm{surf}^4}{\Pi_3'}, \quad [5]$$

respectively. We solve Eqs. (4)-(5) numerically and determine their end state dynamical behavior (steady state or limit cycle) following the procedure described in the main text ("Numerical Method for Equation Solving"). The only difference is that we use an explicit fifth order Runge-Kutta method to integrate (1).

We run 10^5 parameter combinations generated via Latin hypercube sampling of $\log \Pi_1'$, $\log \Pi_2'$, $\log \Pi_3'$, ΔT_cloud, and β. We find all parameter combinations reach steady state and show no variability. Therefore, we conclude that non-zero lag d is required for our model to generate variability.

We provide the physical intuition for why the lag d cannot be zero or too small for oscillations to occur. The lag d effectively holds back the restoring force in the system—the formation of clouds that cool the surface—while the driving force—the rapid vapor release from a hot surface—remains active. The driving force pushes the system away from equilibrium, and if d is too small, the restoring force is released too soon, pulling the system back before it has moved far from equilibrium. This limits the oscillation amplitude and can even prevent oscillations altogether.

Solutions not converging to steady state or detectable limit cycle

When $\beta > 1$, we encounter a small fraction of parameter combinations (about 2%) in the parameter space spanned by Figure 3 that do not converge to our numerical definitions of steady state or a limit cycle even after running the model 10× longer than the majority of cases take to converge ($3000d$ vs $300d$). Figure S5 shows an example of one of these non-converging solutions encountered while constructing Figure 3. The three colors show three numerical approaches: (1) our default numerical setup, (2) our default numerical setup except the numerical solver's relative tolerance is set 10% lower, and (3) our default numerical setup except we use a different method for integration (2). All three numerical approaches show consistent erratic variability, which suggests this solution property is likely not due to our numerical implementation.

It is computationally prohibitive to integrate large numbers of these erratic solutions much past $3000d$ due to high memory requirements from over 10 million numerical integrator steps. (We tested different numerical solvers but did not identify one that could produce significantly fewer steps.) Therefore, we conservatively exclude solutions not converging to steady state or a detectable limit cycle from consideration of observational consistency in Figure 3. Inspection of multi-dimensional parameter dependencies and numerical convergence tests indicate that short period detected limit cycles ($P \lesssim 0.8d$) are also associated with this variability. We therefore conservatively exclude limit cycles with $P < 0.8d$ when $\beta > 1$ as well. These exclusions have very minor implications for our results as they exclude less than 0.2% of solutions from inclusion in Figure 3.

Even though our coupled system of equations is two dimensional, because our model includes a delay differential equation, it can exhibit dynamical behaviors of higher dimensional systems, including possibly chaos (3). Of future interest is further examining whether the magma temperature-cloud feedback could produce chaotic behavior when $\beta = \tau_\mathrm{LW}/\tau_\mathrm{SW} > 1$. Such

behavior could also potentially explain the seemingly uncorrelated near-IR and mid-IR brightness temperatures observed by (4) (c.f. Fig. S5B).

In Figure S6, we examine the dynamical regime of our model as a function of β for two sets of other model parameters. For each value of β, we plot values of $T_{\rm surf}$ when $\tau_{\rm SW}$ is equal to its fixed point $\tau^*_{\rm SW}$ over the last $50d$ of simulation. (The simulation terminates due to reaching convergence to an end state (steady state or limit cycle) or reaching $3000d$.) In steady state, $T_{\rm surf}(\tau^*_{\rm SW})$ has one unique value, the fixed point $T^*_{\rm surf}$. For a "simple" limit cycle, $T_{\rm surf}(\tau^*_{\rm SW})$ has two unique values straddling $T^*_{\rm surf}$. More than two unique values of $T_{\rm surf}(\tau^*_{\rm SW})$ for a given parameter set suggests a more complex limit cycle or chaos.

The parameter set visualized in Figure S6A shows a typical behavior of our model as β varies: the dynamical regime does not change. The parameter set visualized in Figure S6B shows a rare behavior of our model: dynamical regime sensitivity to β with erratic variability emerging for $\beta > 1$. Figure S7 shows time series of $T_{\rm surf}$ for six of the β values in Figure S6B.

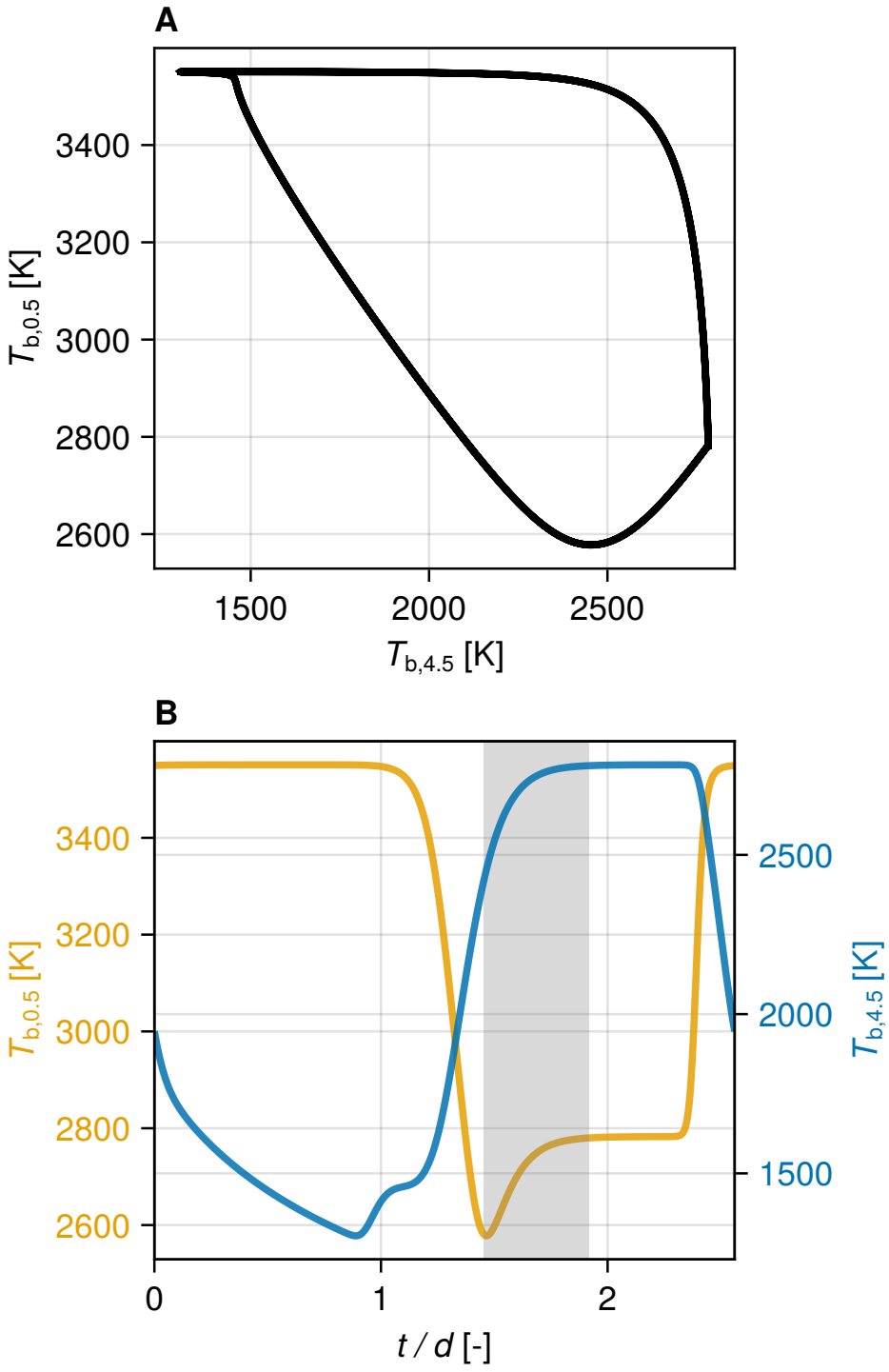

Fig. S1. An example limit cycle with an out-of-phase oscillation qualitatively similar to the JWST/NIRCam observations of (4) (see Fig. S3). (A) Phase diagram of the 0.5 µm brightness temperature $T_{b,0.5}$ and the 4.5 µm brightness temperature $T_{b,4.5}$. (B) Time series (in non-dimesionalized time t/d) of $T_{b,0.5}$ (yellow, left vertical axis) and $T_{b,4.5}$ (blue, right vertical axis) over one oscillation period. The gray shading highlights the time of the out-of-phase oscillation. Model parameters: $\Pi_1 = 93.3\ \mathrm{Pa}^{-1}$, $\Pi_2 = 18.8$, $\Pi_3 = 439\ \mathrm{kg\,s^{-3}\,K^{-1}}$, $\Delta T_{\mathrm{cloud}} = 28.5\ \mathrm{K}$, and $\beta = 2.36 \times 10^{-3}$.

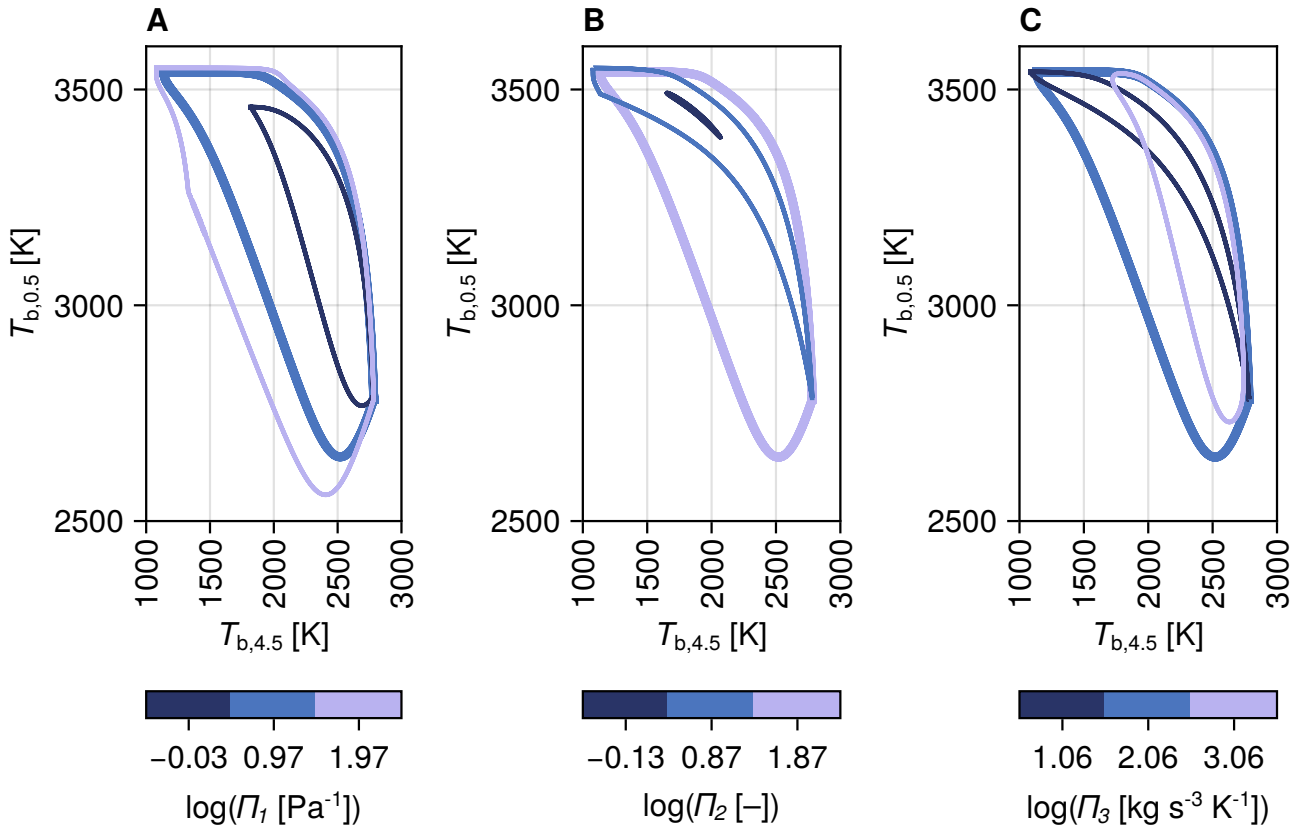

Fig. S2. Figure 2B (phase diagram of the 4.5 µm brightness temperature $T_{b,4.5}$ and the 0.5 µm brightness temperature $T_{b,0.5}$) with perturbed bulk parameters: (A) shortwave scatterer (or longwave absorber) productivity Π_1, (B) loss efficiency of shortwave scatterer (or longwave absorber) Π_2, and (C) thermal inertia Π_3. In each panel, three curves are shown only differing by their Π value (as labeled in colorbar) with the thickest line representing the default parameter value used in Figure 2. Model parameters (unless modified as indicated by colorbar) follow Figure 2: $\Pi_1 = 9.47$ Pa^{-1}, $\Pi_2 = 74.2$, $\Pi_3 = 115$ kg s^{-3} K^{-1}, $\Delta T_{cloud} = 177$ K, and $\beta = 0.143$.

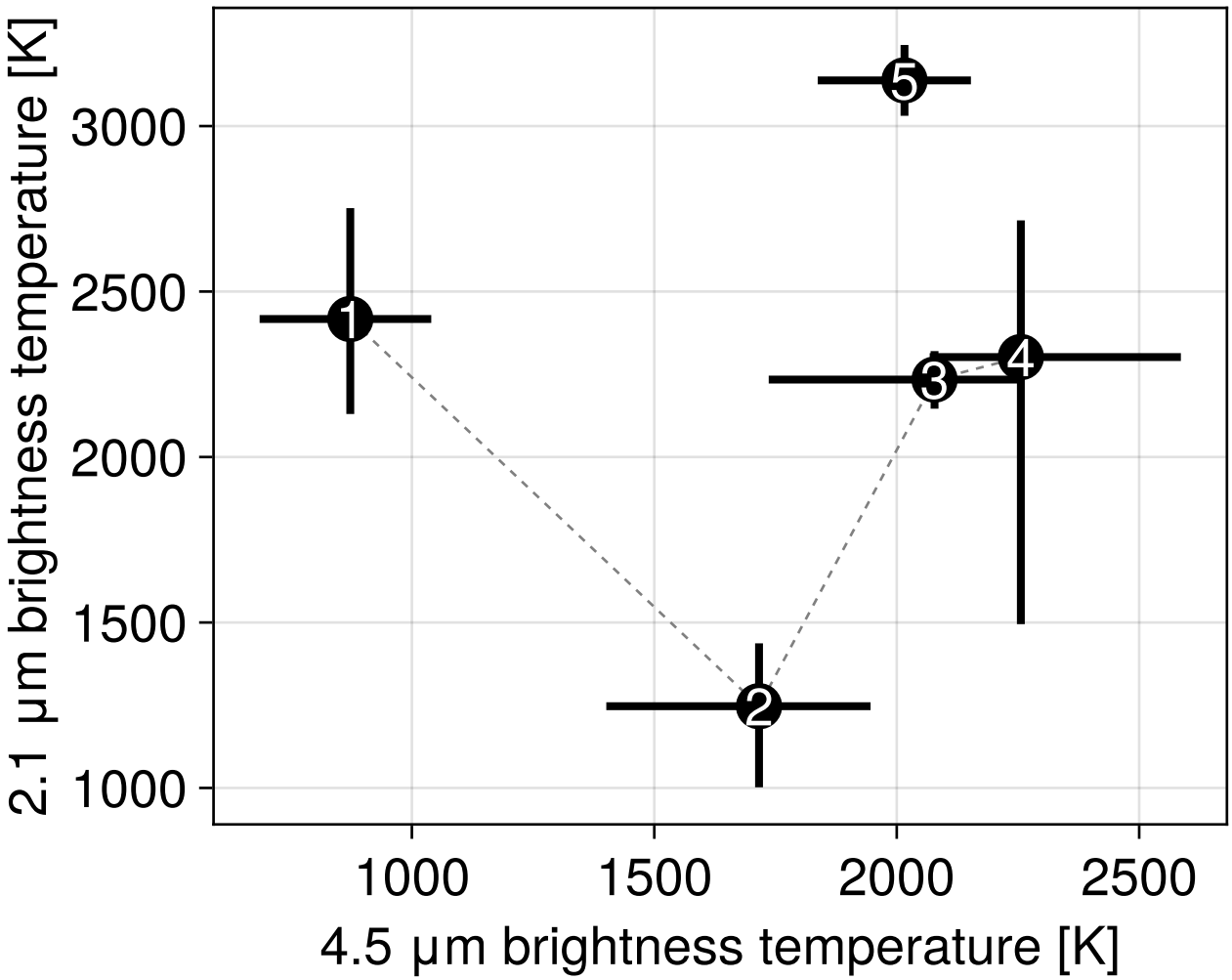

Fig. S3. JWST/NIRCam 2.1 µm brightness temperature vs 4.5 µm brightness temperature from Patel et al. (4) Table 1. Error bars correspond to 1 standard deviation in retrieved brightness temperature. Numeric labels on scatter points correspond to "visit" eclipse number. Dashed lines connect the four eclipse measurements taken within a week.

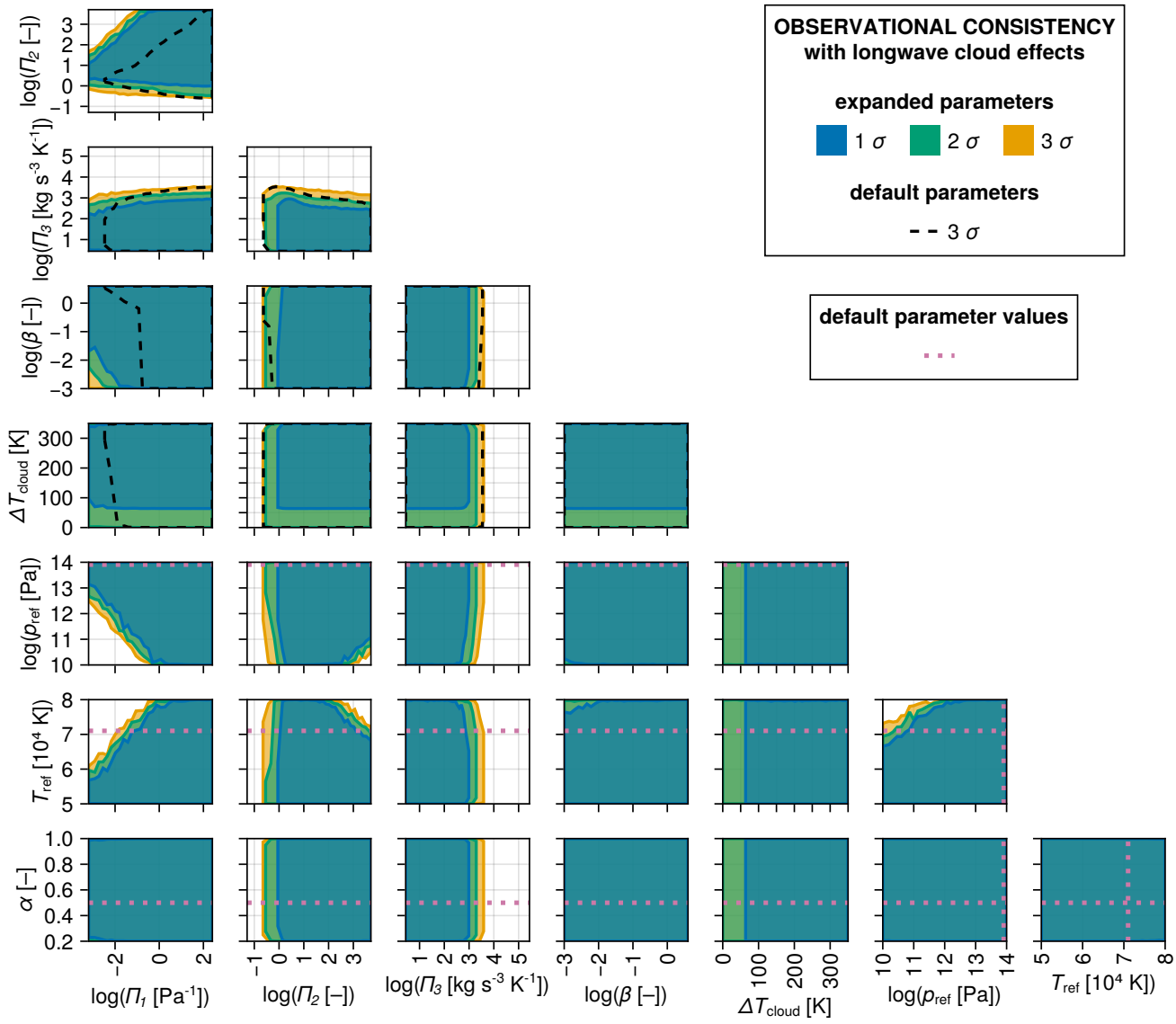

Fig. S4. Similar to Figure 3 with additional parameter sensitivity tests for three parameters fixed in the main text: reference pressure p_{ref}, reference temperature T_{ref}, and albedo parameter α. Parameter ranges capable of simultaneously reproducing the upper and lower bounds of Spitzer and JWST 4.5 µm brightness temperature observations within one, two, and three times the measurement uncertainty (σ). The shading and solid contours show the model with longwave cloud effects with additional p_{ref}, T_{ref}, and α parameter perturbations. Different colors indicate different levels of consistency. For comparison, the dashed black contours in the first four rows show the model (with longwave cloud effects) as presented in Figure 3 at 3σ model-observation consistency. The dotted pink lines in the last three rows show the default parameter values of p_{ref}, T_{ref}, and α in Figure 3.

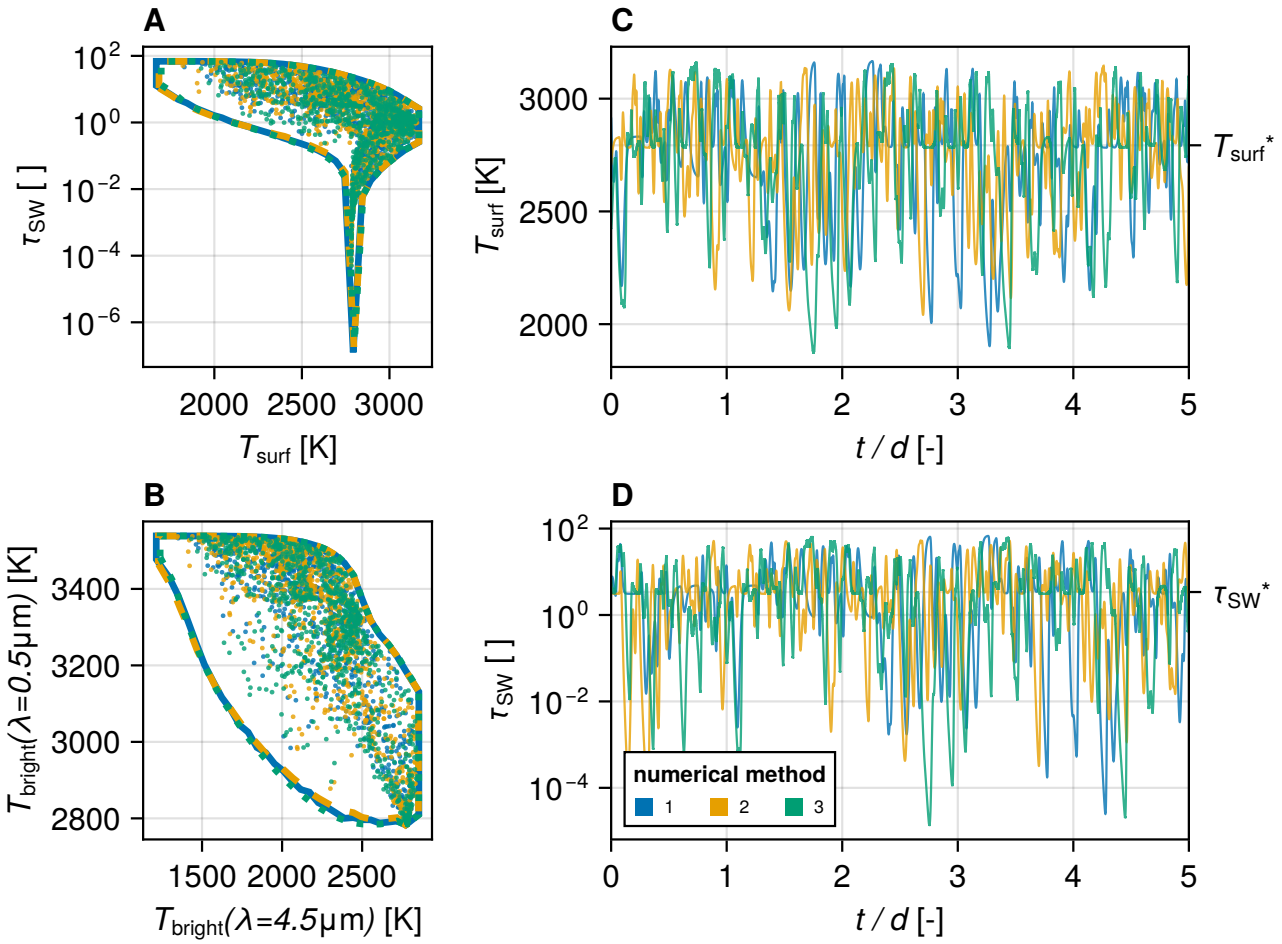

Fig. S5. An example of a model simulation not converging to steady state or a detectable limit cycle. Colors indicate three different numerical methods (as labeled in panel D): (1) our default numerical setup (blue), (2) our default numerical setup except the numerical solver's relative tolerance is set 10% lower (yellow), and (3) our default numerical setup except we use a different method for integration (green; 2). (A) Phase space of shortwave optical depth τ_{SW} vs surface temperature T_{surf}. Scatter points show 1,000 random points from the last 2,000 d of simulation. The thick line encircling the scatter points shows the maximum extent of the phase space. (In addition to color, different numerical methods also have different line styles to see their overlap.) The three methods approximately share the same attractor. (B) Like Panel A except phase space for the 0.5 µm brightness temperature $T_{b,0.5}$ vs 4.5 µm brightness temperature $T_{b,4.5}$. (C) T_{surf} vs non-dimensionalized time t/d. (D) τ_{SW} vs t/d. Model parameters: $\Pi_1 = 1.75$ Pa^{-1}, $\Pi_2 = 377$, $\Pi_3 = 28.8\ \mathrm{kg\ s^{-3}\ K^{-1}}$, $\Delta T_{cloud} = 323$ K, and $\beta = 3.31$.

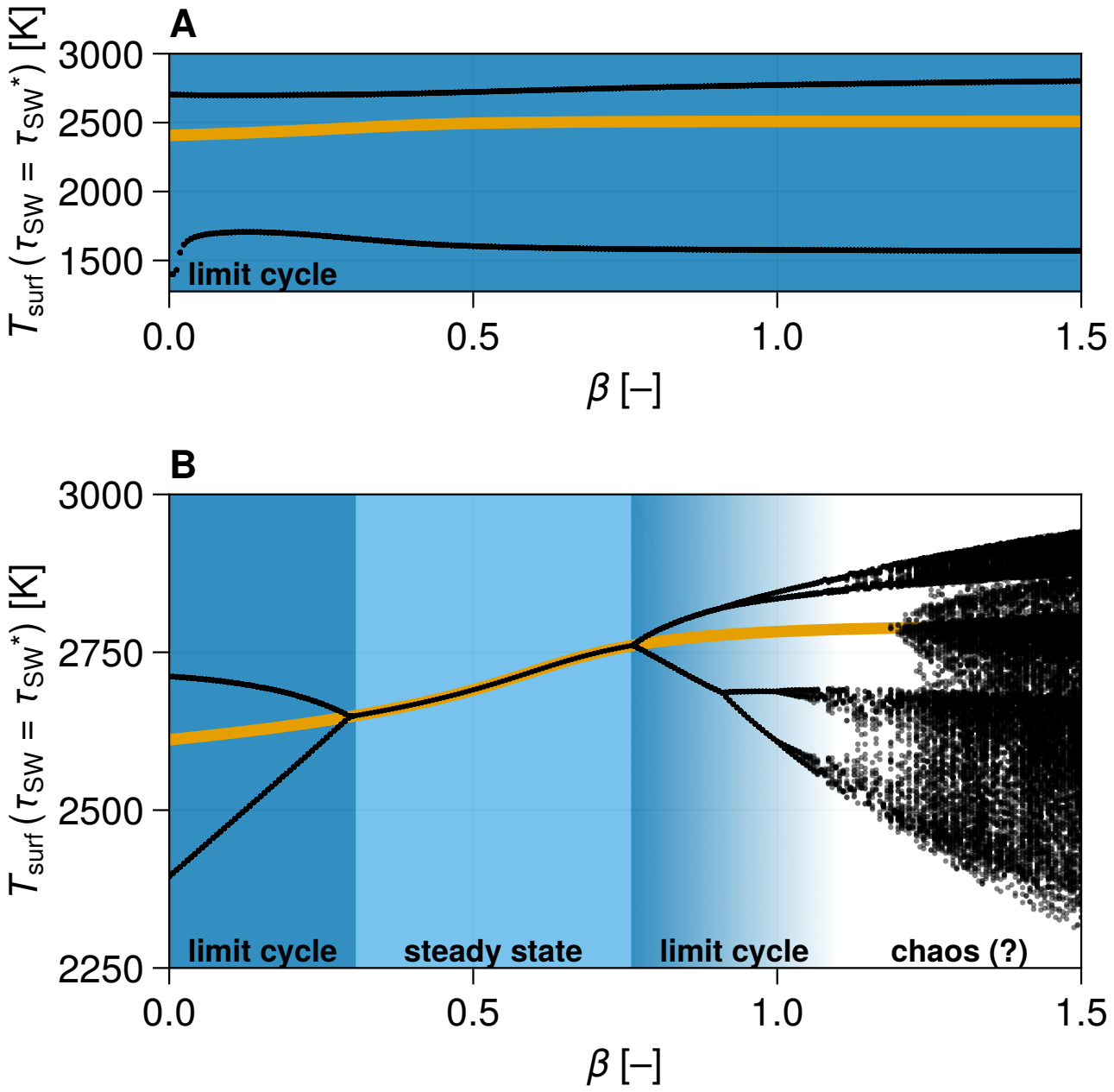

Fig. S6. Example bifurcation diagrams for variable β (ratio of longwave optical depth to shortwave optical depth) and all other model parameters fixed. Black scatter points show values of surface temperature T_{surf} when shortwave optical depth τ_{SW} is equal to its fixed point τ_{SW}^* for the final $50d$ of simulation vs β. The solid yellow line shows the surface temperature fixed point T_{surf}^* vs β. As β varies, the system can switch dynamical regimes (indicated by different background color shading as labeled). Panel A shows a typical limited dependence on β across most of the parameter space explored. Panel B shows an example of a rare case where solutions begin to behave erratically as β increases. After a series of period doubling bifurcations, chaotic behavior appears to occur for $\beta \gtrsim 1.05$. Panel A model parameters: $\Pi_1 = 9.47\ \mathrm{Pa}^{-1}$, $\Pi_2 = 74.2$, $\Pi_3 = 115\ \mathrm{kg\,s^{-3}\,K^{-1}}$, and $\Delta T_{cloud} = 177$ K. Panel B model parameters: $\Pi_1 = 1.75\ \mathrm{Pa}^{-1}$, $\Pi_2 = 377$, $\Pi_3 = 28.8\ \mathrm{kg\,s^{-3}\,K^{-1}}$, and $\Delta T_{cloud} = 323$ K. Note, these diagrams only show behavior when β varies but all other models parameters are fixed; therefore, they are not reflective of Figure 3 (which varies in 5 dimensions rather than 1).

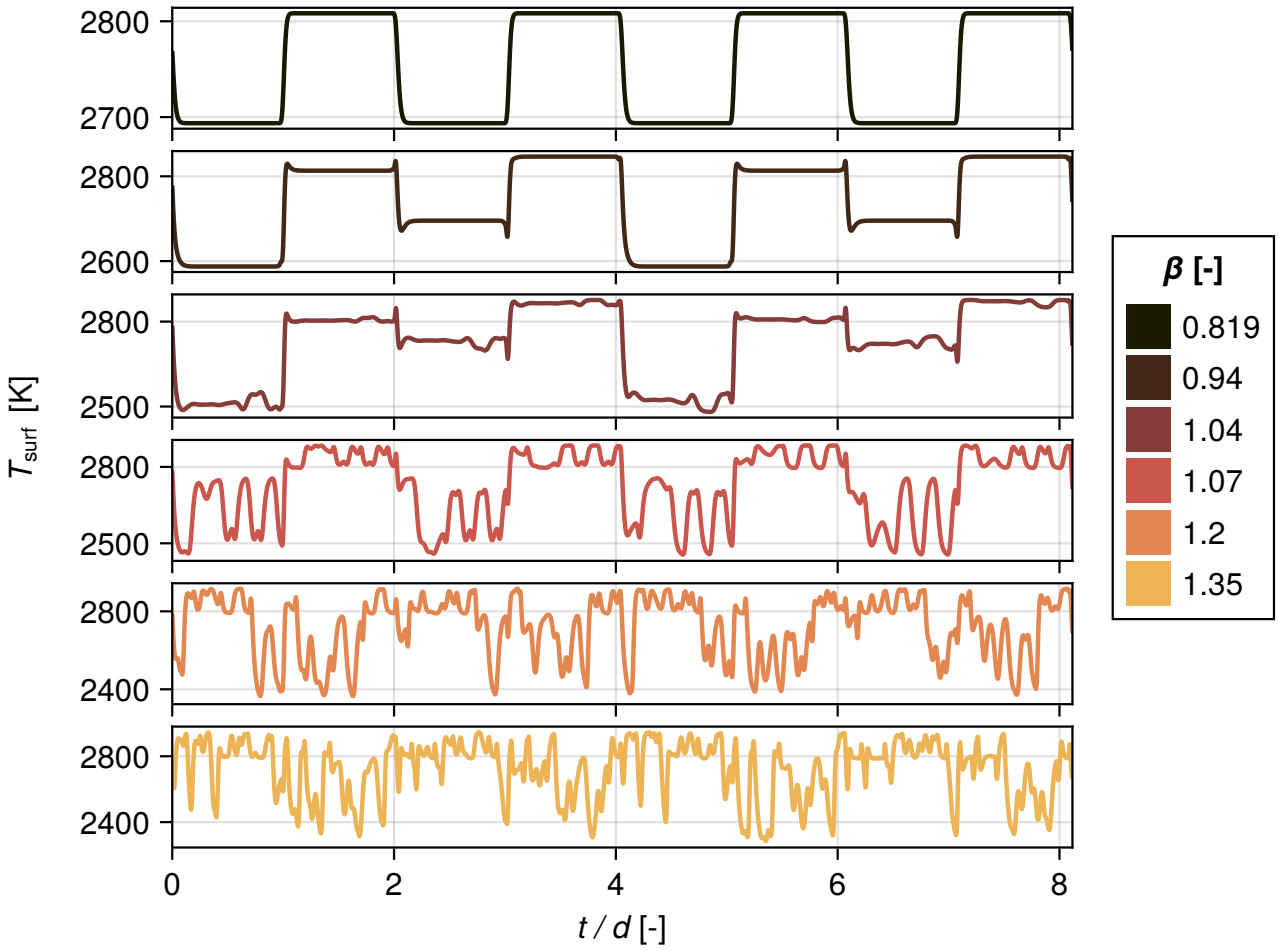

Fig. S7. Surface temperature T_{surf} vs non-dimensionalized time t/d for six different values of β (ratio of longwave optical depth to shortwave optical depth) and fixed other parameters. Values of β are labeled by color and increase downward. The time series duration shown is four periods of the top row limit cycle ($\beta = 0.819$). Other model parameters (same as Figure S6: $\Pi_1 = 1.75\,\text{Pa}^{-1}$, $\Pi_2 = 377$, $\Pi_3 = 28.8\,\text{kg}\,\text{s}^{-3}\,\text{K}^{-1}$, and $\Delta T_{\text{cloud}} = 323\,\text{K}$.

Table S1. Estimated bounds for individual model parameters that constitute Π_1, Π_2, and Π_3

Parameter	Physical meaning	Value or bounds	Note
R^*	universal gas constant	8.3144 $\mathrm{J\ mol^{-1}\ K^{-1}}$	
g	gravitational acceleration	22 $\mathrm{m\ s^{-2}}$	From ref. (5)
M_v	molar mass of the cloud-forming vapor	44 $\mathrm{g\ mol^{-1}}$	For SiO
M_air	mean molar mass of the background atmosphere	28–44 $\mathrm{g\ mol^{-1}}$	Considering CO, $\mathrm{N_2}$, and $\mathrm{CO_2}$, supported by ref. (6)
ρ_c	density of cloud particles	2100–3600 $\mathrm{kg\ m^{-3}}$	Lower bound: for SiO, upper bound: for $\mathrm{Mg_2SiO_4}$
r_c	mean radius of cloud particles	0.2–30 $\mu\mathrm{m}$	From ref. (7)
T_0	representative atmospheric temperature	675–3000 K	Lower bound: stratospheric skin temperature based on the lowest observed nightside brightness temperature, upper bound: the highest surface temperature
η	dynamic viscosity of the background atmosphere	4.6×10^{-5}–8.0×10^{-5} $\mathrm{kg\ m^{-1}\ s^{-1}}$	Lower bound: for $\mathrm{N_2}$ or CO at 1500 K, upper bound: for $\mathrm{CO_2}$ at 3000 K, from refs. (8, 9)
c_p	specific heat capacity of magma	1090–2360 $\mathrm{J\ kg^{-1}\ K^{-1}}$	Lower bound: for FeO melt, upper bound: for MgO melt, from ref. (10)
ρ_m	density of magma	2180–2800 $\mathrm{kg\ m^{-3}}$	Lower bound: for rhyolitic magma, upper bound: for basaltic magma
H_mix	thickness of the mixed layer of the surface magma ocean	1–1000 m	Upper bound referenced from refs. (11, 12)
d	time delay between high surface temperature and accelerated cloud formation	1 hour to 10 days	Lower bound: surface-to-cloud vertical transport timescale, upper bound: horizontal transport timescale to encircle the planet
k_1	scale factor accounting for uncertainties in the scaling for the increase rate of cloud optical depth	0.001–1	Lower bound: limited supersaturation, particle nucleation barriers, subsaturated near-surface atmosphere, mixing with ambient air
k_2	scale factor accounting for uncertainties in the scaling for the residence time of cloud	0.1–100	Lower bound: non-spherical particles (13), cloud depth uncertainty, upper bound: particle growth, cloud depth uncertainty (14)

Table S2. Numerical convergence test

summary statistic	quantity	magnitude of relative error
maximum	min(T_{surf})	2.48×10^{-3}
mean	min(T_{surf})	1.50×10^{-5}
maximum	max(T_{surf})	1.27×10^{-3}
mean	max(T_{surf})	7.51×10^{-6}
maximum	min($T_{\text{b,4.5}}$)	2.56×10^{-3}
mean	min($T_{\text{b,4.5}}$)	1.81×10^{-5}
maximum	max($T_{\text{b,4.5}}$)	1.06×10^{-3}
mean	max($T_{\text{b,4.5}}$)	8.39×10^{-6}

To perform a numerical convergence test, we model 10^5 parameter combinations generated via Latin hypercube sampling of log Π_1, log Π_2, log Π_3, ΔT_{cloud}, and β twice: once with our default numerical setup and once with 10% of the default relative and absolute tolerance. The magnitude of relative error (|RE|) for quantity x is calculated from a model simulation run with default numerics (subscript "default") and a model simulation (with the same parameters) run with 10% of the default tolerances (subscript "10% tol.") via

$$|\text{RE}| = \left| \frac{x_{\text{default}} - x_{10\% \text{ tol.}}}{x_{10\% \text{ tol.}}} \right| . \quad [6]$$

The summary statistic (mean or maximum) is calculated from all runs converging to steady state or detectable limit cycle in our default numerical setup (as required for inclusion in Figure 3). (We exclude the erratic variability runs as we do not necessarily believe they have converged.) The quantity is calculated over the last $100d$ of simulation (i.e., the same procedure for generating Figure 3).

References

1. C Tsitouras, Runge–kutta pairs of order 5 (4) satisfying only the first column simplifying assumption. *Comput. & Math. with Appl.* **62**, 770–775 (2011).
2. A Kværnø, Singly diagonally implicit runge–kutta methods with an explicit first stage. *BIT Numer. Math.* **44**, 489–502 (2004).
3. H Wernecke, B Sándor, C Gros, Chaos in time delay systems, an educational review. *Phys. Reports* **824**, 1–40 (2019).
4. J Patel, et al., Jwst reveals the rapid and strong day-side variability of 55 cancri e. *Astron. & Astrophys.* **690**, A159 (2024).
5. V Bourrier, et al., The 55 cancri system reassessed. *Astron. & Astrophys.* **619**, A1 (2018).
6. R Hu, et al., A secondary atmosphere on the rocky exoplanet 55 cancri e. *Nature* **630**, 609–612 (2024).
7. D Powell, X Zhang, P Gao, V Parmentier, Formation of silicate and titanium clouds on hot jupiters. *The Astrophys. J.* **860**, 18 (2018).
8. RC Weast, MJ Astle, WH Beyer, *CRC Handbook of Chemistry and Physics.* (CRC Press), (1986).
9. Crane Company, *Flow of Fluids through Valves, Fittings and Pipe.* (Crane Company), (1988).
10. R Lange, A Navrotsky, Heat capacities of fe2o3-bearing silicate liquids. *Contributions to Mineral. Petrol.* **110**, 311–320 (1992).
11. Y Lai, J Yang, W Kang, Ocean circulation on tide-locked lava worlds. i. an idealized 2d numerical model. *The Planet. Sci. J.* **5**, 204 (2024).
12. Y Lai, W Kang, J Yang, Ocean circulation on tide-locked lava worlds. ii. scalings. *The Planet. Sci. J.* **5**, 205 (2024).
13. K Ohno, S Okuzumi, R Tazaki, Clouds of fluffy aggregates: How they form in exoplanetary atmospheres and influence transmission spectra. *The Astrophys. J.* **891**, 131 (2020).
14. W Rossow, Cloud microphysics: Analysis of the clouds of earth, venus, mars and jupiter. *Icarus* **36**, 1–50 (1978).